Association Aéronautique et Astronautique de France

57th 3AF International Conference on Applied Aerodynamics
29 – 31 March 2023, Bordeaux - France

AERO2023-17-MUTANGARA

A UNIFIED PARTIAL PRESSURE FIELD AND VELOCITY DECOMPOSITION APPROACH TOWARD IMPROVED ENERGETIC AERODYNAMIC FORCE DECOMPOSITIONS

N.E. Mutangara, D.S. Sanders, and P. Laskaridis
Cranfield University, Bedford, MK430AL, United Kingdom, Email: ngonidzashe.e.mutangara@cranfield.ac.uk, d.s.sanders@cranfield.ac.uk, P.Laskaridis@cranfield.ac.uk
P.L. Hart and S. Schmitz
Pennsylvania State University, University Park, Pennsylvania, 16802, Email: puh69@psu.edu, sus52@psu.edu

ABSTRACT

Drag decomposition through energy and exergy-based methods has been shown to have a variety of advantages. One of these is identifying and quantifying the recoverable energy within a flow field. This describes the available energy that can be used to produce thrust through systems such as boundary layer ingestion. Another advantage highlighted from prior work is that the velocity decomposition approach can split the flow field into its isentropic and non-isentropic contributions. This provides region-specific formulations for drag assessment, wherein the isentropic field is associated with contributions originating from the bulk flow and the non-isentropic field with the shear layer. This paper aims to assess the performance of a modified form of the velocity decomposition approach for transonic flows. This modification involves unification with partial pressure field analysis, which provides better flow field separability due to the added decomposition of the pressure field.

1. NOMENCLATURE

A	= total anergy deposition rate [W]
$A_{\nabla T}$	= thermal anergy deposition rate [W]
A_{Φ}	= viscous anergy deposition rate [W]
A_w	= wave anergy deposition rate [W]
c	= chord length [m]
c_d	= drag coefficient quantity
e	= mass-specific internal energy [J kg $^{-1}$]
D	= drag force [N]
dV	= volume element of the control volume
$\delta(\ )$	= variation of parameter relative to the
$\dot{\varepsilon}_{th}$	= thermal exergy deposition rate [W]
$\dot{E}_a$	= axial kinetic energy deposition rate [W]
$\dot{E}_v$	= transverse kinetic energy deposition rate [W]
$\dot{E}_p$	= pressure-work deposition rate [W]
$\dot{E}_m$	= mechanical energy deposition rate [W]
EWC	= exergy waste coefficient [-]
$\mathbf{F}$	= integrated force quantities [N]
M	= Mach Number
$\hat{\mathbf{n}}$	= unit normal vector, out-of-control volume
Θ	= volumetric power [W]
Φ	= viscous dissipation rate [W]
ρ	= fluid density [kg/m^3]
p	= static pressure [Pa]
PER	= potential for energy recovery [-]
P_t	= total pressure [Pa]
Re	= Reynolds number
s	= mass-specific entropy [J. kg $^{-1}$. K $^{-1}$]
S_{ref}	= reference area [m^2]
dS	= surface element of the control volume
T	= Temperature [K]
$\bar{\boldsymbol{\tau}}$	= viscous stress tensor
u, v, w	= perturbation velocities [m/s]
$\mathbf{V}$	= fluid velocity $(V_\infty + u)\hat{x} + v\hat{y} + w\hat{z}$
V^2	= fluid speed squared $= \mathbf{V}\cdot\mathbf{V}$

Subscripts

E	= non-dissipative flow quantity
i	= lift-induced drag quantity
o	= outer-control-volume surface
phy	= physical exergy quantity
pr	= profile drag quantity
$shock$	= shock wave associated quantity
μ	= dissipative flow quantity
w	= wave drag quantity
VII	= viscous inviscid interaction
∞	= freestream quantity

2. INTRODUCTION

External aerodynamic analysis through computational fluid dynamics (CFD) provides flow field solutions by solving the Navier-Stokes equations within a flow domain. Classical aerodynamic analysis shows that particular flow regions can be accurately modelled using

comparatively simpler formulations governed by the flow physics of the region [1,2]. For example, the shear layers can be modelled through the boundary-layer defect equations, while the remainder of the bulk flow can be modelled using the Euler formulations. These equations can be solved simultaneously through a technique known as viscous inviscid interaction (VII)[2], which allows for the solutions of these equations to be combined through an iterative process until a converged solution is obtained for the entire flow field. The composite solution obtained from VII helps to highlight that real viscous flows can be described as a superposition comprising of an Euler and defect flow field. Aguirre [3], who introduces the velocity decomposition approach, acknowledges this aforementioned flow decomposition. This approach assists in splitting a composite CFD flow field into isentropic (inviscid) and non-isentropic (viscous) parts, allowing for region-specific drag formulations. The non-isentropic formulation quantifies drag originating from the shear layers, and the isentropic quantifies the bulk flow associated drag contributions.

Implementation of this approach relies on the assumption that the isentropic static pressure field can be approximated by the real viscous flow static pressure field, which affects the accuracy and subsequent interpretation of decomposition terms. However, the partial pressure field (PPF) method can be combined with the velocity decomposition approach [3] to overcome this assumption, thereby improving accuracies in energy/exergy-based analyses. The objective of this paper is to demonstrate the accuracy of this unification accuracy in complex flow studies, including shockwave formation and lift production.

3. MATHEMATICAL MODELS AND NUMERICAL METHODOLOGY

3.1. Velocity Decomposition and Partial Pressure Field Unification

The velocity decomposition approach described by Aguirre [4] is based on Betz's [5] artificial velocity principle, which approximates the velocity field's behaviour when no loss in the total energy is experienced. Previously, Méheut [6] had introduced a similar velocity decomposition approach that allowed for the evaluation of profile drag using far-field momentum analysis. This method accurately analysed the profile drag and could be used in experimental studies in wind tunnels by evaluating downstream wake data. However, Aguirre [4] later identified that Méheut's [6] approach would not be valid when coupled with exergy-based analysis, as it assumes that the transverse velocities are isentropic throughout the entire flow field. This is only true for flow outside the BL and wake zones, i.e., bulk flow. Within the shear layers, all velocity components consist of isentropic and non-isentropic components[1]. To address this, Aguirre introduced a new procedure for velocity decomposition, which obtains the isentropic flow components of the velocity, density and temperature from the isentropic flow equations and ideal gas law. This methodology relied on two primary assumptions, the first being that the static pressure of the real-viscous flow is equivalent to the isentropic static pressure. Following this assumption, obtaining the magnitude of the isentropic velocity is possible. The second assumption is that the direction of the isentropic velocity vector is the same as that of the real-viscous flow field at all points in the domain. PPF analysis [7–9] is incorporated into the methodology to approximate the isentropic pressure field. PPF analysis considers the pressure field as a superposition of an Euler and dissipative pressure governed by the Poisson equations (1).

$$\begin{aligned} \nabla^2 p_E &= \nabla\cdot\left(-\rho\left(\mathbf{V}\cdot\nabla\right)\mathbf{V}\right) \quad (\mathrm{a}) \\ \nabla^2 p_\mu &= \nabla\cdot\left(\nabla\cdot\boldsymbol{\tau}\right) \quad (\mathrm{b}) \end{aligned} \tag{1}$$

These equations are solved numerically using ANSYS Fluent©, where the non-dissipative Euler pressure solution provides an alternative means of approximating the isentropic pressure field for substitution into Aguirre's velocity decomposition approach to obtain the isentropic velocity. However, this substitution does not take care of the direction of the isentropic velocity vector, which is similarly assumed to be in the bulk flow direction [4]. As the flow field can now effectively be separated into two constitutive parts, this naturally extends to each part's force contributions, as shown in equation (2). Therefore, the real viscous flow drag can be represented as a superposition of the dissipative drag, originating from the shear layers and the non-dissipative drag associated with the bulk flow.

$$\mathbf{F}_{RVF} = \underset{\text{shear-layer}}{\mathbf{F}_\mu} + \underset{\text{bulk flow}}{\mathbf{F}_E} \tag{2}$$

The momentum, energy, and exergy-based drag and drag power formulations in equations (3) are obtained using the first principal derivations based on the Euler flow field.

For non-lifting scenarios, the non-dissipative field is expected to behave similarly to an Euler flow, which would have a drag contribution of zero. However, in this instance, the Euler flow reconstruction represented through the non-dissipative field results in a non-zero contribution due to the BL and wake having a finite

[1] Isentropic and non-isentropic are analogous to non-dissipative and dissipative as mentioned in the work of Schmitz et al. [7,19]

displacement and momentum thickness that would not be observed for an actual Euler flow[7,8]. This formulation is beneficial for lifting flows as it provides a unique way of quantifying the additional drag contribution linked to the airfoil's downwash, i.e., lift-induced drag [3].

$$\mathbf{F}_E = -\iint_S \begin{bmatrix} p_{G,E}\mathbf{n} \\ +\left(\mathbf{V}_E - \mathbf{V}_\infty\right)\rho_E \mathbf{V}_E \cdot \mathbf{n} \end{bmatrix} dS \quad (a)$$
$$\mathbf{F}_E \cdot \mathbf{V}_\infty = \dot{E}_{phy_E} = \begin{cases} \dot{E}_{m_E} + \Theta_E & (b) \\ \dot{E}_{m_E} + \dot{\varepsilon}_{th_E} & (c) \end{cases} \quad (3)$$

Lastly, the non-dissipative drag can be quantified through the formulations in equation (3). Equation 3(a) shows the non-dissipative force obtained via the momentum equation, whilst (3)(b) and (c) show the non-dissipative drag power obtained through mechanical energy and exergy formulations, respectively. It then becomes possible through equation (2) to obtain the dissipative drag by taking the difference between the Euler and real viscous flow quantities.

3.2. Shockwave Treatment

The primary focus of this work is the extension of the unified velocity and partial pressure decomposition approach to transonic flows, which is examined through two case studies taken from literature [4,9]. For these analysis it is essential to note that the development of shockwaves adds additional drag. Drela [10] proposes quantifying the wave drag power contribution using mechanical energy methods by measuring the wave pressure work and kinetic energy deposition rate crossing the Side Cylinder ($\dot{E}_w$).

$$\dot{E}_w = \iint_{S_O^{SC}} \begin{bmatrix} p - p_\infty \\ +\frac{1}{2}\rho\left(u^2 + v^2 + w^2\right) \end{bmatrix} V_n \, dS \quad (4)$$

This evaluation method, however, is highly dependent on pressure work and kinetic energy of the wave system crossing the Side Cylinder.

As a result, if a large control volume is used with no pressure work or kinetic energy interacting with the side cylinder, the resulting $\dot{E}_w$ will be zero. Therefore the wave drag evaluated through $\dot{E}_w$ becomes less accurate as the size of the transverse plane is increased. On the other hand, wave drag assessment methods introduced by Kusonose [16,17], Arntz [11–14] and Aguirre[19] provide a more robust method of wave drag assessment using CFD solutions. This research will look into various methods of estimating the wave drag using CFD solutions in order to develop a more robust method of calculating wave drag using power balance analysis that is less sensitive to changes in the transverse plane size compared to $\dot{E}_w$.

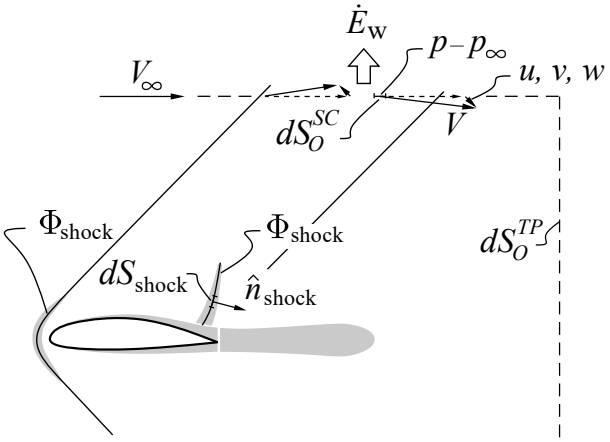

Figure 1: Surface and normal vector definition for theoretically discontinuous shockwaves adapted from [10]

Shock waves are treated as adiabatic, inviscid flow field discontinuities in this work, which are characterised by an infinitesimal width labelled S_{shock} in Figure 1, similarly done in [11]. Therefore to numerically assess shockwave effects within finite volume codes, it is necessary to realise that the entire flow domain is continuous. As such, the volumetric shockwave region V_{shock} must be isolated, which is delineated by the outline of the shaded portion in Figure 1 and encloses the shockwave surface S_{shock}. The numerical identification of this region is made through flow feature identification methods discussed in further detail in Section 4.2. After identifying the shockwave region, the drag contribution can be evaluated using the wave anergy formulation shown in equation (5).

$$\mathrm{A}_w = T_\infty \iint_{S_{\mathrm{shock}}} \rho \delta s \mathbf{V} \cdot \hat{\mathbf{n}}_{\mathrm{shock}} \, dS = D_{\mathrm{wave}} V_\infty \quad (5)$$

As this evaluation is associated with the anergy field, it is directly related to exergy analysis [11] and, as a result, can be extended to power balance analysis [10,15] through the internal energy equation (6).

$$\begin{aligned} &\oiint_S \left[\rho\delta e + p_\infty\right]\mathbf{V}\cdot\mathbf{n}\, dS \\ &= \iint_{S=S_O+S_{\mathrm{shock}}} \left[\rho\delta e + p_\infty\right]\mathbf{V}\cdot\mathbf{n}\, dS = \Phi + \Theta \\ &= \dot{\varepsilon}_{th} + \mathrm{A}_{total} \end{aligned} \quad (6)$$

The internal energy equation allows for an alternative formulation of the pressure-volume work related to the thermal exergy and total anergy. As the wave anergy is a

component of the total anergy this implies that this alternative formulation includes the wave anergy contribution, as shown in equation (7)(a). However, this can easily be reduced to obtain the dissipative pressure-volume work by using the dissipative thermal exergy instead of the real viscous flow quantity, as shown in equation (7)(b).

$$\begin{aligned}\Theta_{\text{indirect}} &= \dot{\varepsilon}_{th} - \Phi + \underbrace{\mathrm{A}_w + \mathrm{A}_{\nabla T} + \mathrm{A}_{\Phi}}_{\mathrm{A}_{total}} \\ &= \dot{\varepsilon}_{th} - \dot{\varepsilon}_{\Phi} + \mathrm{A}_w + \mathrm{A}_{\nabla T} \quad (\mathrm{a}) \\ \Rightarrow \Theta_{\text{indirect},\mu} &= \dot{\varepsilon}_{th,\mu} - \dot{\varepsilon}_{\Phi} + \mathrm{A}_w + \mathrm{A}_{\nabla T} \quad (\mathrm{b})\end{aligned} \tag{7}$$

It should be noted that this formulation assumes wave anergy is only related to pressure-volume work. Additionally, the formulation relies on the accuracy of the chosen method to evaluate the airfoil wave drag. As a result, three methods are selected for the case studies presented here to quantify the wave drag and compare their ability to capture this phenomenon for various flow scenarios.

The first method calculates wave drag via the wave using exergy-based analysis [11]. As shown in equation (8), wave drag is obtained indirectly by subtracting the viscous and thermal anergy from the total anergy. This method assumes the total domain anergy is categorised into three sources, i.e., $\mathrm{A}_{total} = \mathrm{A}_w + \mathrm{A}_{\Phi} + \mathrm{A}_{\nabla T}$.

$$D_{\text{wave}} V_\infty = \mathrm{A}_w = \mathrm{A}_{total} - \left(\mathrm{A}_{\Phi} + \mathrm{A}_{\nabla T}\right) \tag{8}$$

The second method applies Arntz's [11–14] surface integral total anergy formulation shown in equation (9) applied to the shockwave wake region depicted in Figure 2(c). This method exploits the idea behind Kusonose's [16,17] profile drag decomposition, which considers that aerodynamic flows consist of two distinct sources of entropy. The first is the boundary and wakes, whilst the second is the shockwave region. As a result, the wave drag can be estimated through the *entropy drag* [18] originating from the shockwave region.

$$D_{\delta s} V_\infty = A_{\text{total}} = T_\infty \iint_{S_O} \rho \delta s \left(\mathbf{V} \cdot \mathbf{n}\right) \, dS \tag{9}$$

The third and final method introduced by Aguirre [19] is a modification of Arntz's surface integral approach, which previously computed the wave drag through surface integration of the anergy crossing a surface enclosing the shockwave. Aguirre's modified approach applies the divergence theorem to obtain a volume integral formulation for wave anergy, as shown in equation (5).

$$\begin{aligned} D_{\text{wave}} V_\infty = \; & \\ \mathrm{A}_w = & \underbrace{T_\infty \iint_{S_{\text{shock}}} \rho \delta s \mathbf{V} \cdot \tilde{\mathbf{n}} \, dS}_{\text{Arntz method}} \\ = & \underbrace{\iiint_{V_{\text{shock}}} \nabla \cdot \left(T_\infty \rho \delta s \mathbf{V}\right) \, dV}_{\text{Aguirre method}} \end{aligned} \tag{10}$$

3.3. Energy Recovery Quantification Performance Metrics

A significant advantage of the component decompositions introduced by energy and exergy-based methods is their ability to identify the recoverable energy within the flow. From an exergy-based perspective, the exergy waste coefficient (EWC) [11–13] is used, which quantifies the total recoverable energy present within the flow, including both mechanical and thermal energy contributions. This differs from the energy-based potential for energy recovery factor (PER) [15] which only considers the mechanical energy within the flow as recoverable and views the remainder of the thermal energy as a loss contributing to the total mechanical energy loss within the domain.

Two significant modifications are made to the recoverable energy formulations, i.e., EWC and PER. The first modification considers only dissipative terms to evaluate the recoverable energy [20]. For energy-based analysis, this entails including the dissipative pressure-volume work as part of the total mechanical energy loss. Additionally, the drag power denominator used for comparison is the converged dissipative drag power, which is taken when this value stabilises at a single quantity. One chord length downstream from the airfoil trailing edge has been considered sufficient for the case studies.

$$\begin{aligned} EWC_\mu &= 1 - \frac{\mathrm{A}_{\text{total}}}{D_{\mu_{1c}} V_\infty} \\ PER_\mu &= 1 - \left(\frac{\Phi + \Theta_{\mu_{\text{indirect}}}}{D_{\mu_{1c}} V_\infty} \right) \end{aligned} \tag{11}$$

The second modification pertains mainly to PER. As transonic flows are studied, it becomes necessary to update the formulation to include the modified pressure-volume work expression in equation (7) which contains the shockwaves contribution through the wave anergy. As a result, the wave-dependent contribution is included in the formulation presented in equation (11).

4. NUMERICAL CFD SIMULATION SETUP

Various manipulations of the far-field momentum, energy and exergy methods have been performed to provide a unified flow field decomposition approach that utilises both velocity decomposition and PPF analysis. This paper verifies the numerical implementation and assesses the performance of these formulations for drag evaluation of transonic airfoils. Additionally, this paper takes particular interest in enhancing understanding concerning the quantification of recoverable energy for complex flow scenarios, including shockwave formation and lift production.

4.1. Boundary and Operating Conditions

Two case studies, taken from literature, were considered for the analyses conducted. The first case study consisted of a non-lifting NACA 0012 airfoil at zero degrees angle of attack, Mach number 0.80 and a Reynolds number of 3×10^6.

The second case study assessed a lifting NACA 0012 airfoil at a Mach number 0.70 and a Reynolds number of 9×10^6 at an angle of attack of 3.04. These cases were modelled in a classical C-H domain with pressure farfield and outlet boundaries at the peripheries and a no-slip wall representing the transonic airfoil. The near-wall cell mesh refinement ensured the y^+ was kept below 0.5 for compatibility with partial pressure field analysis.

As a requirement for solving the dissipative and Euler pressure Poisson equations, the domain boundary conditions were set following the work of Schmitz et al. [7,8,19]. The farfield was set as a Dirichlet boundary condition, wherein the Euler pressure was set to equal the freestream static pressure. The outlet and airfoil walls were both taken as Neumann boundaries. The gradient of the Euler pressure normal to the outlet was set to zero, and at the airfoil surface where the no-slip condition was enforced, it naturally resulted in the state where $\nabla p_E = 0$. Lastly, the dissipative pressure gradient was set to equal the shear stress tensor divergence at the walls and zero normal to the outlet, respectively.

4.2. Flow Feature Identification

To break down the airfoil's drag based on flow physics, it is necessary to identify the regions of influence of the shockwave, boundary layer and wake. Shockwaves are additional flow mechanisms contributing to the airfoil's overall drag in transonic analyses, making it a more complex test case than subsonic flow.

A total pressure identifier ($P_t / P_{t\infty}$) [20] is used to isolate the boundary layer's viscous wake and shock wake regions, as shown in Figure 2(a). This is accompanied by a viscous wake and boundary layer identifier introduced by Sanders and Laskaridis [15] provided in equation (12) which isolates the viscous and shock wake regions shown in Figure 2(b) and (c).

$$\varepsilon = \left(\frac{\mu+\mu_t}{\mu}\right)\left[\frac{(\nabla\cdot\boldsymbol{\tau})\cdot\mathbf{V}}{\left|p(\nabla\cdot\mathbf{V})\right|}\right] \qquad (12)$$

(a) Combined shock wake, viscous wake and boundary layer

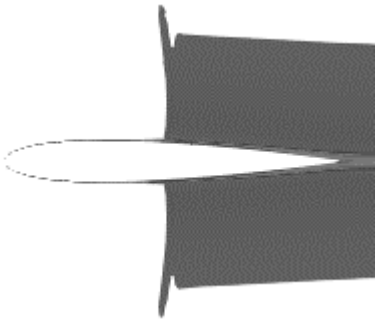

(b) Viscous wake and boundary layer

(c) Shock wake

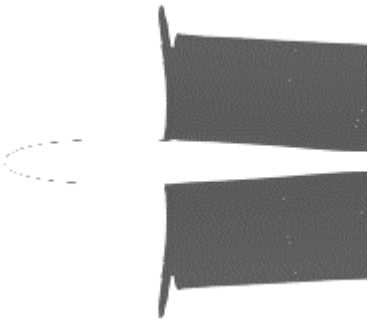

Figure 2: Transonic airfoil isolated flow regions for profile, viscous and wave drag evaluation

5. NUMERICAL CASE STUDIES

5.1. Non-lifting Airfoil Analysis

This case study features a NACA 0012 transonic non-lifting airfoil. The drag is investigated using momentum, energy and exergy-based analysis, all of which with flow field decomposition employed through the partial pressure field and velocity decomposition approaches [4]. In addition, the flow field decomposition allows for an adequate assessment of the profile drag via dissipative field analysis.

Theoretically, this field identifies flow mechanisms

within the domain that act as sources of entropy generation. However, as shown in Figure 3, a portion of the profile drag is contained within the non-dissipative field known as viscous inviscid interaction [8]. The non-dissipative physical exergy[2] $\dot{E}_{phy_E}$ allows this drag contribution to be quantified using both energy and exergy analysis through equations (3)(b) and (c), respectively. For clarity, the evaluation of this term has been restricted to the wake as it does not exhibit the same cumulative behaviour over the body as the dissipative field components.

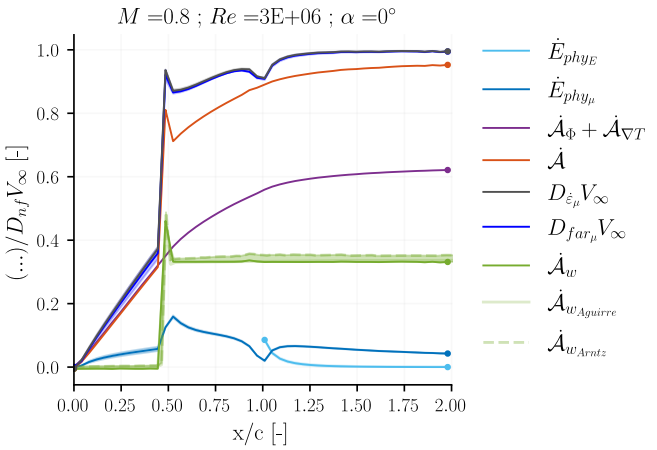

Figure 3: Non-lifting transonic airfoil exergy-based dissipative drag component breakdown at various Trefftz plane locations

Previous work from [21] demonstrates that the non-dissipative field has no contribution toward the recoverable energy as flow mechanisms associated with this field all self-recover as they follow an isentropic path. As a result, the recoverable energy can be quantified through the dissipative field. As such, energy recovery can be thought of as preventing entropy generation by utilising available energy within the flow before it is irreversibly lost to the surroundings. According to Kusonose [16] the most significant sources of entropy production for transonic flows are the BL/wake and shockwave regions. Exergy-based analysis aids in highlighting the flow regions where available energy is present and quantifies its contribution.

For example, the solid black line in Figure 4 represents the total profile drag contribution, it can be observed that two wake regions exist, the first being attributed to the shockwave region, which extends into the bulk flow and the second to the viscous wake region. Figure 3's exergy analysis highlights that the shockwave's drag contribution is related to the anergy field. As a result, the energy within the shockwave's wake has no potential for energy recovery to produce useful work. Drag from the BLs and wakes, on the other hand, contains mechanical and thermal exergy, shown in Figure 4(b), which can be recovered using mechanical and thermal energy devices such as BLI propulsors and heat exchangers. The EWC in equation (6) was used to quantify this recoverable energy yielding a value of 11%.

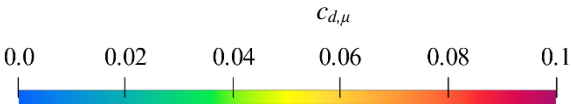

(a) Airfoil viscous and shockwave wake regions

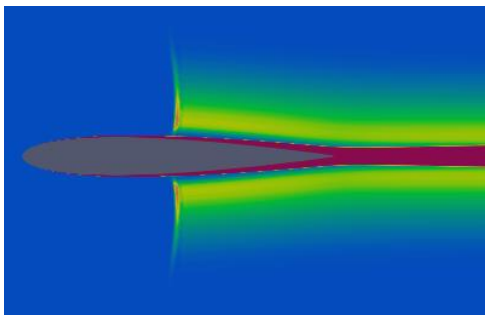

(b) Enhanced wake region behind trailing edge

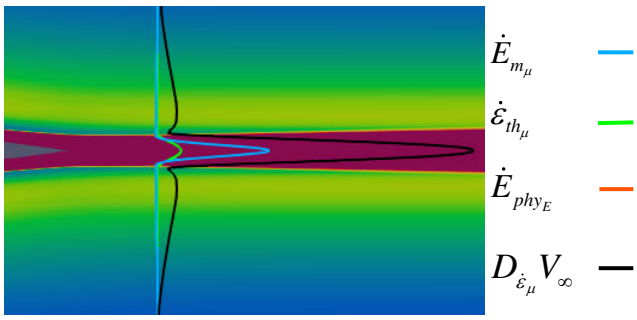

Figure 4: Non-lifting transonic airfoil qualitative wake energy and drag density visualisation

Figure 3 depicts a discontinuous increase in dissipative physical exergy at the region where shock formation begins, followed by a monotonic decrease. This occurs due to the thickening of the boundary layer and increased turbulence across the shock. These effects collectively lead to the observed decrease in physical exergy.

As shown in Figure 4, increasing the Mach number increases the thermo-compressibility effects, which increases the thermal exergy $\dot{E}_{th}$ within the wake. As the production of thermal exergy, so does its dissipation through thermal mixing, which is captured by the thermal anergy shown in Figure 3. The viscous anergy's

[2] The physical exergy is characterised as a combination of the mechanical and thermal exergy contributions

contribution to the total drag power decreases as the shockwave's strength increases due to the intensification of the thermo-compressibility losses. This is due to the increased wave anergy, which contributes significantly to airfoil drag.

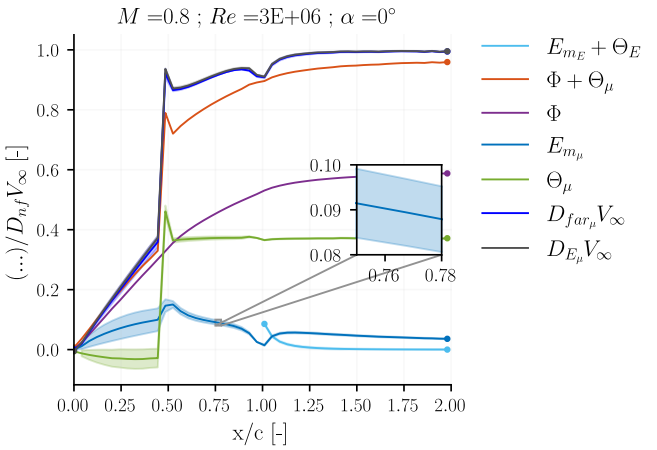

Figure 5: Non-lifting transonic airfoil energy-based dissipative drag component breakdown at various Trefftz plane locations

Figure 5 depicts the dissipative flow field power balance-based drag power analysis. The components are reported by the average value of the unified and velocity decomposition approaches and accompanied by an interval band whose upper bound is provided by the unified approach and the lower bound by the velocity decomposition alone, illustrated in the zoomed-in insert of the dissipative mechanical energy in Figure 5. This analysis aimed to compare the performance of the alternative pressure-volume work formulation and test the accuracy of the overall modified formulation for drag decomposition. The alternative power balance formulation accurately quantifies drag over the airfoil and agrees closely with the momentum analysis used for comparison. Furthermore, this analysis allowed for the evaluation of PER using the modified formulation in equation (6), which yielded a value of 10%, indicating a 1% difference with the EWC. This confirms that the mechanical exergy is the primary contributor toward recoverable energy, as shown in Figure 4(b)'s qualitative wake energy analysis.

5.2. Lifting Airfoil Analysis

The purpose of this section is to demonstrate the applicability of the unified decomposition approach for transonic lifting flows and to estimate the recoverable energy using the modified PER and EWC formulations. These flows are naturally more complex as they combine lift and shockwave effects.

The first observation in Figure 6 is similar to the previous observation of the non-lifting airfoil. The dissipative physical exergy is seen to rise and then increase abruptly across the shock, followed by a gradual decay.

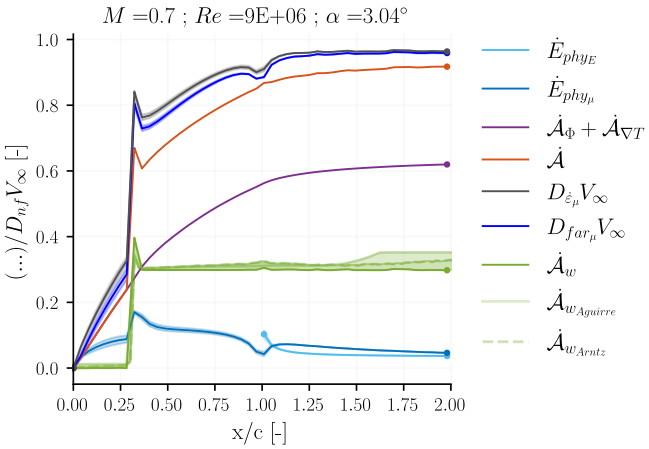

Figure 6: Lifting transonic airfoil exergy-based dissipative drag component breakdown at various Trefftz plane locations

The wave anergy trends exhibit similar behaviour to those previously observed, with good agreement between the surface and volume-integral methods. An important note, however, is that the non-lifting scenario has a more precise delineation between the downstream viscous and shockwave wake regions. As a result, less wake mixing occurs, resulting in a more consistent downstream wave anergy evaluation, as shown in Figure 3. However, due to the mixing of the viscous and shockwave wake, the value of wave anergy obtained via flow feature identification shows a slight uptick at around 1.5 chord lengths, as shown in Figure 6. On the other hand, the wave anergy obtained indirectly using equation (8) shows a constant contribution, as expected. This highlights that the uptick in wave anergy demonstrated by the surface and volume integral evaluation methods is purely a limitation brought about by the flow feature and volume identification procedure.

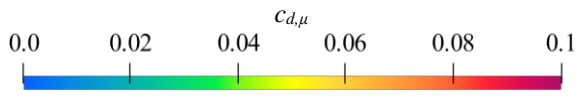

(a) Airfoil shockwave and viscous wake regions

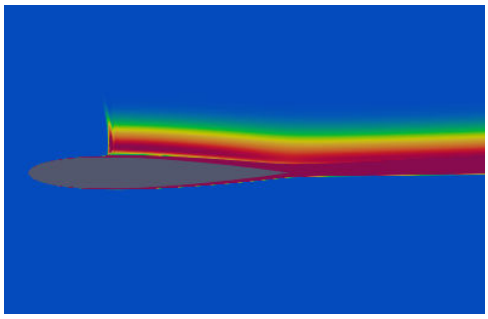

(b) Enhanced wake region behind trailing edge

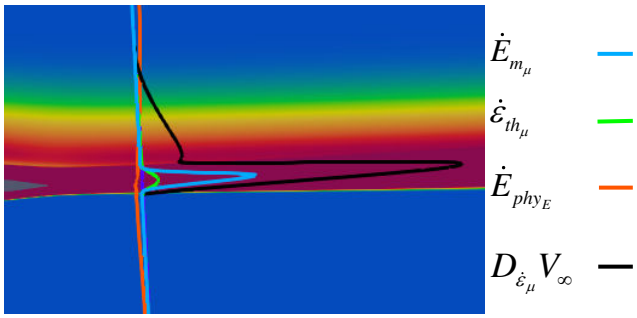

Figure 7: Lifting transonic airfoil qualitative wake energy and drag density visualisation

Figure 7(b) shows an energy contribution outside the wake due to mechanical energy being deposited into the downstream flow as a result of lift production, which is not seen in the non-lifting test case in Figure 4(b). Furthermore, outside the viscous wake region, there is a significant contribution to the drag density, primarily representing the wave drag. The viscous wake contributes significant thermal exergy due to the high thermo-compressibility. As previously seen in Section 5.1, mechanical energy is also contained in this region, which adds to the total physical exergy within the wake, resulting in an EWC ≈ 10%.

Finally, the power balance method was used to decompose the airfoil drag power. Figure 8 depicts the total mechanical energy loss calculated using viscous dissipation and dissipative pressure-volume work. This was used to calculate PER using equation (6), which yielded a value of ≈ 9%. Because of the higher Reynolds number, the lower recoverable energies compared to the non-lifting airfoil are to be expected. The higher the Reynolds number, the greater the viscous losses, reducing the amount of recoverable energy imparted to the downstream flow.

As a lifting airfoil is considered in this instance, the energy imparted to the flow due to lift production was also calculated using non-dissipative mechanical energy and pressure-volume work. In exergy-based analysis, this is analogous to the non-dissipative physical exergy. A zoomed-in insert of the dissipative mechanical energy similar to the non-lifting test case is provided to demonstrate the relative difference between the unified approach and the velocity decomposition method. The unified approach again provided the upper bound of the flow component, resulting from including the dissipative pressure contribution in evaluating dissipative mechanical energy, increasing the amount of energy imparted to the flow.

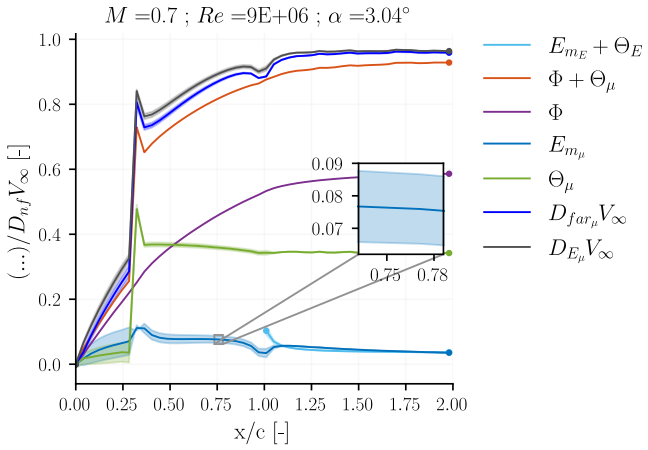

Figure 8: Lifting transonic airfoil energy-based dissipative drag component breakdown at various Trefftz plane locations

6. DISCUSSION

The primary motivation of the first section of work was to identify the sensitivity through which wave drag is calculated using the side cylinder evaluation methods. It was postulated that as the size of the control volume was increased, and the distance of the side cylinder from the aerodynamic body and the formed shockwave, the accuracy of the wave drag evaluation through $\dot{E}_w$ would diminish. As a result, this prompted the need for an alternative formulation of wave drag when using mechanical energy methods for large control volumes where the flow perturbation effects caused by the shockwave do not cross the side cylinder and instead cross the transverse plane.

To address this issue, an alternative formulation for pressure-volume work was proposed, relying on unification with exergy-based analysis through the introduction of the internal energy equation. This indirect formulation includes the wave energy term, giving the ability to quantify the total drag of the body without omitting the wave energy contribution when using mechanical energy methods.

The results shown in Table 1 confirm this and show that when the suggested correction to the mechanical energy equations is not employed, the difference between the total drag obtained via mechanical energy, represented in parentheses in Table 1, and exergy-based analysis is equivalent to the magnitude of the wave drag. As verification, the farfield approach is also used where it can be shown that the value obtained using farfield momentum analysis provides a good agreement with the exergy-based total drag. This confirms that the evaluation of transonic flows with classical mechanical energy analysis omits the wave drag contribution for large control volumes as the side cylinder contribution diminishes to 0.

When the suggested correction associated with the indirect evaluation of the pressure-volume work is used, it can be observed that there is good agreement between the mechanical energy, exergy and farfield solutions, all agreeing to well within a 5% difference. It should be noted, however, that this evaluation assumes that the effects associated with the wave drag are strictly related to the pressure-volume work alone. This assumption still requires assessment and will be the driving factor for future work focusing on a mechanical energy-based formulation of wave drag.

Additionally, this work aimed to improve the accuracy of energy/exergy-based analyses by unifying the velocity decomposition approach with partial pressure field analysis. The proposed method uses the Euler pressure field, which provides an approximation of the inviscid static pressure field. By combining this with the isentropic and ideal gas equations, as well as the velocity decomposition approach, it becomes possible to more accurately reconstruct the dissipative and non-dissipative flowfields. Furthermore, the isentropic velocity can be used to reconstruct the non-dissipative flowfield through the ideal gas law. Incorporating PPFs into the velocity decomposition approach allows a more accurate breakdown of the flow field into its dissipative and non-dissipative portions. This is achieved as the dissipative losses arising from the pressure field are now accounted for.

It is commonly understood that drag can be split into various components, such as profile, lift-induced, and wave drag. Profile drag originates within the boundary layers and wake, whereas lift-induced drag is due to lift production, and wave drag is characteristic of transonic flows with shockwave formation. The use of various methods, including near-field, far-field, energy and exergy-based techniques, as shown in Table 1, help provide a clear view of the various components contributing to drag. For instance, the near-field dissipative drag is lower than the dissipative drag obtained with the other subsequent methods. This is because farfield momentum, energy, and exergy methods consider contributions from both profile and wave drag effects within the dissipative field. Therefore, through this comparison, the near-field quantity aids in highlighting the additional contribution which is not explicitly related to the profile drag for the far-field methods, i.e. wave drag. To separately evaluate the wave drag contribution, the methods presented by Kusonose [16,17], Arntz [11–14] and Aguirre[19] can be used, whose formulations are shown in equations (8) — (10).

On the other hand, the non-dissipative near-field drag captures both the wave drag and a portion of the form drag due to viscous inviscid interaction and drag due to lift. Far-field methods can be used to separately evaluate the wave drag and lift-induced drag, which allows for identifying the viscous inviscid interaction drag reported in Table 1. Furthermore, the summation of the viscous and viscous inviscid interaction drag gives a near-field profile drag value that agrees well with the profile drag values provided by the farfield momentum, energy and exergy-based methods. It is important to note that the near-field wave drag quantities were obtained through the farfield approaches mentioned prior. However, PPFs can be utilised to quantify the wave drag through the procedure outlined in [9] which was not conducted in this work. This presents another avenue for future work to extend and refine the analyses performed.

Lastly, regarding energy and exergy-based analysis, the flowfield decomposition helps identify region-specific drag contributions, where the dissipative field is associated with the profile drag and the non-dissipative field with the lift-induced drag. Unification with PPFs improves the identification of recoverable energy and lift-induced drag. The prior static pressure assumption considered all contributions from the pressure field as isentropic, resulting in an under-approximation of quantities such as the recoverable energy evaluated through the dissipative field. This is illustrated through the zoomed-in inserts of the dissipative mechanical energy in Figure 5 and 8, where the upper bound of the interval band was provided by the unified approach and the lower bound by the velocity decomposition approach. Quantifying the dissipative pressure contributions allows for a more accurate representation of drag mechanisms originating from the dissipative and non-dissipative flowfields.

Table 1: Aerodynamic force decomposition comparisons reported in drag counts ($c_d \times 10^{-4}$)

M ;α°; Re	Near-field				Far-field				Power Balance				Exergy			
	173				177				175(114)				173			
	$c_{d,\mu}$	$c_{d,E}$			$c_{d,\mu}$	$c_{d,E}$			$c_{d,\mu}$	$c_{d,E}$			$c_{d,\mu}$	$c_{d,E}$		
0.80; 0°	76	97			177	0			175(114)	0			173	0		
3×10^6		$c_{d,i+VII}$	$c_{d,w}$		$c_{d,pr}$	$c_{d,w}$			$c_{d,pr}$	$c_{d,w}$			$c_{d,pr}$	$c_{d,w}$		
		39	58		119	58			114	61			115	58		
	146				144				144 (99)				144			
	$c_{d,\mu}$	$c_{d,E}$			$c_{d,\mu}$	$c_{d,E}$			$c_{d,\mu}$	$c_{d,E}$			$c_{d,\mu}$	$c_{d,E}$		
0.70; 3.04°	68	78			140	4			140 (95)	4 (4)			140	4		
9×10^6		$c_{d,i+VII}$	$c_{d,w}$		$c_{d,pr}$	$c_{d,w}$			$c_{d,pr}$	$c_{d,w}$			$c_{d,pr}$	$c_{d,w}$		
		33	45		96	44			95	45			96	44		
		$c_{d,VII}$	$c_{d,i}$													
		29	4													

7. CONCLUSIONS

In this work, the breakdown of airfoil drag is performed using farfield momentum, energy and exergy-based analysis to verify their numerical implementation. The adoption of exergy-based analysis, particularly for transonic flows, allows for the evaluation of shockwave drag contributions through the wave anergy following the procedure detailed by Arntz. As this phenomenon is associated with the anergy field, it is understood that energy associated with this mechanism cannot be utilised to produce useful work. To identify the portion of energy which indeed can be utilised, flow field decomposition methods become essential. The work performed here shows these decomposition methods can be coupled with partial pressure field analysis, which allows for a linear decomposition of the pressure field into its dissipative and non-dissipative contributions. By coupling this with the velocity decomposition approach, fewer assumptions can be taken to separate the flow field into dissipative and non-dissipative parts while also allowing for a more complete depiction of the energy imparted to the flow. For instance, energy imparted to the bulk flow was quantified through the non-dissipative field largely associated with lift-induced drag contributions. It is also known that energy associated with this field self-recovers and does not offer any recoverable energy as the path followed by the fluid elements is isentropic. This entails that the region which offers an energy recovery potential is concentrated to the viscous wake and BL regions. From the flow field decomposition, it is possible to assess the energy imparted to this region using the dissipative field through the physical exergy shown in Figure 3 and 6 or alternatively through the exergy waste coefficient or potential for energy recovery factors given in equation (11).

The work performed here also explores the extension of the flow decomposition approach to power balance analysis. Through this, it is possible to evaluate the dissipative pressure-volume work, which identifies the thermo-compressibility loss contributions within the domain. For power balance analysis, all thermo-compressibility effects (which include both thermal exergy and anergy) are considered as losses as mechanical energy devices are not able to harness their available energy content. This largely implies that only the dissipative mechanical energy is regarded as recoverable through mechanical energy devices such as boundary layer/wake-ingesting propulsors.

Furthermore, using Arntz's approach for shockwave treatment, the proposed derivations in this work link the wave anergy with the mechanical energy-based pressure-volume work term through the internal energy equation discussed in Section 3. This link provides a modified formulation for the dissipative pressure-volume work as

well as the potential for energy recovery in the presence of shockwaves.

The unified approach presented in this work offers a means of aerodynamic performance assessment where the various components of aerodynamic drag can be identified through near-field, far-field, energy, and exergy-based approaches. Future work will focus on the development of a mechanical energy-based wave drag formulation and an assessment of wave drag using partial pressure fields.

8. REFERENCES

[1] Lock, R. C., and Williams, B. R. "Viscous-Inviscid Interactions in External Aerodynamics." *Progress in Aerospace Sciences*, Vol. 24, No. 2, 1987, pp. 51–171. https://doi.org/10.1016/0376-0421(87)90003-0.

[2] Williams, B. R. "Viscous-Inviscid Interaction Schemes for External Aerodynamics." *Sadhana*, Vol. 16, No. 2, 1991, pp. 101–140. https://doi.org/10.1007/BF02812177.

[3] Mutangara, N. E., Sanders, D. S., Laskaridis, P., Kingdom, U., Hart, P. L., and Schmitz, S. "A Unified Partial Pressure Field and Velocity Decomposition Approach toward Improved Energetic Aerodynamic Force Assessment." *AIAA Journal (Submitted for Review)*, pp. 1–40.

[4] Aguirre, M. A., Duplaa, S., Carbonneau, X., and Turnbull, A. "Velocity Decomposition Method for Exergy-Based Drag Prediction." *AIAA Journal*, Vol. 58, No. 11, 2020, pp. 4686–4701. https://doi.org/10.2514/1.J059414.

[5] Betz, A. *A Method for the Direct Determination of the Wing Section Drag*. Washington, 1925.

[6] Méheut, M., and Bailly, D. "Drag-Breakdown Methods from Wake Measurements." *AIAA Journal*, Vol. 46, No. 4, 2008, pp. 847–862. https://doi.org/10.2514/1.29051.

[7] Schmitz, S. "Drag Decomposition Using Partial-Pressure Fields in the Compressible Navier–Stokes Equations." *AIAA Journal*, Vol. 57, No. 5, 2019, pp. 2030–2038. https://doi.org/10.2514/1.J057701.

[8] Schmitz, S., and Coder, J. G. "Inviscid Circulatory-Pressure Field Derived from the Incompressible Navier–Stokes Equations." *AIAA Journal*, Vol. 53, No. 1, 2015, pp. 33–41. https://doi.org/10.2514/1.J053140.

[9] Hart, P., and Schmitz, S. A Partial Pressure Field For Airfoil Wave Drag. 2022.

[10] Drela, M. "Power Balance in Aerodynamic Flows." *AIAA Journal*, Vol. 47, No. 7, 2009, pp. 1761–1771. https://doi.org/10.2514/1.42409.

[11] Arntz, A. *Civil Aircraft Aero-Thermo-Propulsive Performance Assessment by an Exergy Analysis of High-Fidelity CFD-RANS Flow Solutions*. Ph.D. Dissertation, Université de Lille, Lille,France, 2014.

[12] Arntz, A., and Atinault, O. "Exergy-Based Performance Assessment of a Blended Wing–Body with Boundary-Layer Ingestion." *AIAA Journal*, Vol. 53, No. 12, 2015, pp. 3766–3776. https://doi.org/10.2514/1.J054072.

[13] Arntz, A., and Hue, D. "Exergy-Based Performance Assessment of the NASA Common Research Model." *AIAA Journal*, Vol. 54, No. 1, 2016, pp. 88–100. https://doi.org/10.2514/1.J054127.

[14] Arntz, A., Atinault, O., and Merlen, A. "Exergy-Based Formulation for Aircraft Aeropropulsive Performance Assessment: Theoretical Development." *AIAA Journal*, Vol. 53, No. 6, 2015, pp. 1627–1639. https://doi.org/10.2514/1.J053467.

[15] Sanders, D. S., and Laskaridis, P. "Full-Aircraft Energy-Based Force Decomposition Applied to Boundary-Layer Ingestion." *AIAA Journal*, Vol. 58, No. 10, 2020, pp. 4357–4373. https://doi.org/10.2514/1.J058695.

[16] Kusunose, K., Crowder, J. P., and Watzlavick, R. L. "Wave Drag Extraction from Profile Drag Based on a Wake-Integral Method." *37th Aerospace Sciences Meeting and Exhibit*, No. c, 1999. https://doi.org/10.2514/6.1999-275.

[17] Aguirre, M. A., and Duplaa, S. "Exergetic Drag Characteristic Curves." *AIAA Journal*, Vol. 57, No. 7, 2019, pp. 2746–2757. https://doi.org/10.2514/1.J057985.

[18] Oswatitsch, K. *Gas Dynamics*. Academic Press, 1956.

[19] Hart, P., and Schmitz, S. Application of Partial-Pressure Field Drag Decomposition to the ONERA M6 Wing. 2021.

[20] Aguirre, M. A., and Duplaa, S. "Epsilon V2.0 - User's Manual." 2020.

[21] Aguirre, M., Duplaa, S., Carbonneau, X., and Turnbull, A. A Systematic Analysis of the Mechanical Exergy of an Airfoil by Using Potential Flow , Euler & RANS. 2019.

A unified partial pressure field and velocity decomposition approach toward improved energetic aerodynamic force decomposit

Mutangara, Ngonidzashe E.

2023-03-31

Mutangara NE, Sanders DS, Laskaridis P, et al., (2023) A unified partial pressure field and velocity decomposition approach toward improved energetic aerodynamic force decompositions. In: 57th 3AF Applied Aerodynamics Conference AERO2023, 29-31 March 2023, Bordeaux, France

https://dspace.lib.cranfield.ac.uk/handle/1826/19664